ACS APPLIED MATERIALS & INTERFACES

www.acsami.org Research Article

Novel Biomaterial-Binding/Osteogenic Bi-Functional Peptide Binds to Silk Fibroin Membranes to Effectively Induce Osteogenesis *In Vitro* and *In Vivo*

Ruyin Lyu, Yuping Chen, Yajun Shuai, Jie Wang, Leihao Lu, Qichao Cheng, Jiangfeng Cai, Chuanbin Mao,* and Mingying Yang*

Cite This: *ACS Appl. Mater. Interfaces* 2023, 15, 7673−7685 Read Online

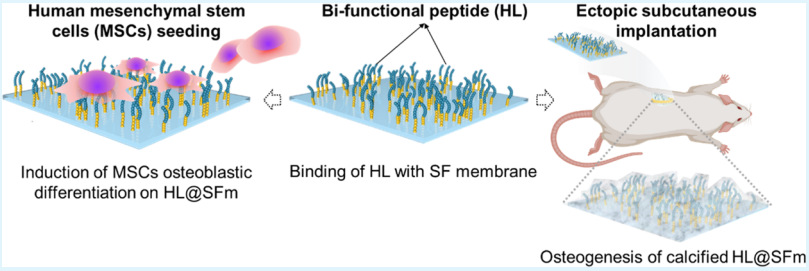

ABSTRACT: Peptides can introduce new functions to biomaterials but their immobilization usually relies on inefficient physical adsorption or tedious chemical conjugation. Using the *Bombyx mori* silk fibroin (SF) membrane (SFm) as a model biomaterial, here, we demonstrate a universal strategy for discovering new peptides that can "stick" to a biomaterial to functionalize it. Specifically, two peptide motifs, one screened by phage display biopanning for binding to the biomaterial (i.e., SF) and another derived from an osteogenic growth factor (i.e., bone morphogenetic protein-2), are fused into a new chimeric peptide that can bind to SFm for more efficient osteogenesis. Theoretical simulations and experimental assays confirm that the chimeric peptide binds to SF with high affinity, facilely achieving its immobilization onto SFm. The peptide enables SFm to effectively induce osteogenic differentiation of human mesenchymal stem cells (MSCs) even without other osteogenic inducers and efficiently stimulate bone regeneration in a subcutaneous rat model in 8 weeks, even without MSC seeding, while not causing inflammatory responses. Since biomaterial-binding peptides can be readily screened using phage display and functional peptides can be generated from growth factors, our work suggests a universal strategy for combining them to seek new peptides for binding and functionalizing biomaterials.

KEYWORDS: *peptides, biomaterials, binding, bone differentiation, mesenchymal stem cells*

1. INTRODUCTION

Repairing bone defects under clinical conditions is majorly limited to the necrosis of osteocytes when bone tissue suffers an injury. However, bone cells lack the ability to regenerate themselves.[1] Mesenchymal stem cells (MSCs) are commonly selected to act as osteoprogenitor cells that can differentiate into osteoblasts and regenerate bone tissue.[2,3] Accordingly, bone tissue engineering (BTE) involving stem cells has increasingly become a promising method for meeting the needs of functional recovery.[4] It is well known that cells, scaffolds, and growth factors (GF) are key elements in successful BTE.[5,6] Among these elements, many scaffold materials have been developed, but there is still a need for an ideal scaffold material that can support cell activities for realizing bone regeneration.

Fortunately, *Bombyx mori* (*B.mori*) silk fibroin (SF) is a promising natural biopolymer as it has been employed in the BTE field due to its unique characteristics such as biodegradability, good biocompatibility, and ease of chemical processing.[7−9] Bone morphogenetic protein-2 (BMP-2), an osteogenic factor, retains a strong biological function on SF biomaterial matrices to promote the differentiation of MSCs into osteoblasts and induce bone tissue regeneration.[10,11] In fact, a 20 amino acid fragment (KIPKASSVPTELSAISTLYL, termed KL) obtained from the BMP-2 sequence determines the physiological functions of directing cell differentiation.[12,13] To immobilize the BMP-2 core sequence on the SF scaffolds, some groups utilized the indirect physisorption strategy to aggregate the peptide,[14,15] or followed tedious procedures for chemically coupling the peptides with them.[16,17] However,

Received: September 28, 2022
Accepted: January 11, 2023
Published: February 3, 2023

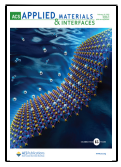

Scheme 1. Schematic Illustration of the Bi-functional Peptide-modified SF Membranes (SFm) to Induce Osteogenic Differentiation of MSCs and Bone Formation in A Rat Subcutaneous Model

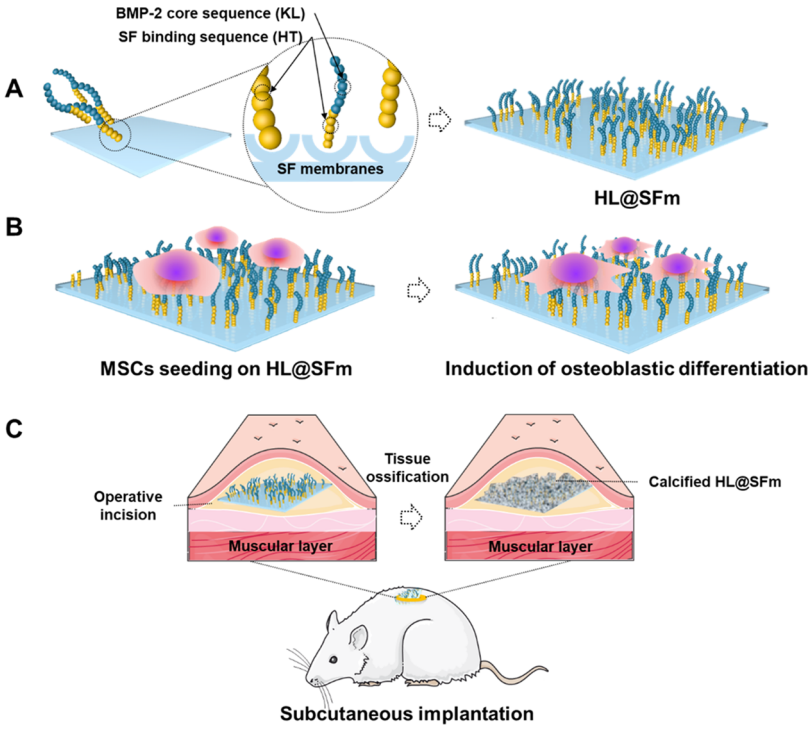

(A) The bi-functional chimeric peptide (HL), made of two motifs (the SF-binding HT and the osteogenic BMP-2-derived KL) with a GGGG linker in between them, presents high binding affinity with SFm, enabling HL to bind to SFm and thus form the HL-coated SFm (HL@SFm). The HT motif binds to SFm while the KL motif protrudes from SFm, allowing the KL to promote osteogenesis. (B) HL@SFm induces the osteogenic differentiation of MSCs without additional differentiation inducers. (C) HL@SFm also induces highly efficient ectopic bone formation with a strong calcification signal in the subcutaneous implantation model, even without MSC seeding.

these strategies cannot avoid the hurdles such as easy shedding and toxicity of cross-linking agents. Therefore, it is important to find out a safe and efficient way to introduce the BMP-2 peptide on the SF scaffold surface.

Interestingly, binding peptide opens a window that links molecules and a scaffold material, allowing the functions of the material surface to be modified.[18] Especially, phage display technology is a direct solution to selecting affinity peptides because from a random phage-displayed peptide library, it can discover the peptide expressed on the outside of a phage virion that can target the given molecule. This peptide binds to the target molecule with high affinity and can be derived from a specific binding phage through multiple rounds of bio-screening.[19,20] Previously, our group has identified and validated an SF-binding affinity sequence[21] (HVAWSWSWNNST, termed HT) that can specifically recognize and attach SF materials through its N-terminal acting as a binding linker (Scheme S1A). Inspired by this SF affinity sequence, we designed a chimeric peptide by adding the BMP-2 core sequence at the C-terminal of the SF affinity sequence. The chimeric peptide is expected to play a role not only in effectively binding to the SF scaffold surface but also working as BMP-2 in mediating osteogenesis.

To verify our speculation, we synthesized the bi-functional chimeric peptide (HVAWSWSWNNSTGGGGKIPKASSVP-TELSAISTLYL, termed HL), a combination of an SF-binding affinity peptide motif (HT for binding to SF) and the BMP-2 core peptide motif (KL for promoting osteogenesis) with a GGGG linker in between (Scheme 1). The SF-binding HT peptide motif was used as a "bridge" to immobilize the BMP-2 core KL peptide on the surface of the SF membranes (SFm), thereby functionalizing SFm to form HL@SFm (Scheme 1A). To achieve this, we incubated the peptide solution with SFm to immobilize HL onto SFm in a layer-by-layer fashion, forming the peptide-modified materials (HL@SFm, Scheme 1A). We found that HL@SFm could induce the differentiation of human MSCs into osteoblasts without other inducers in the medium (Scheme 1B). Finally, HL@SFm was subcutaneously transplanted into rats with or without MSCs seeded to verify its osteogenic ability in vivo (Scheme 1C). We discovered that the membranes could effectively induce bone regeneration even without MSC seeding.

2. MATERIALS AND METHODS

2.1. Preparation of SF Membranes (SFms). The SF membranes were prepared by drop-casting as described previously with slight changes.[22] Briefly, the degummed SF fibers were subjected to salt dissolution, desalination, dialysis, and freeze-drying to obtain regenerated SF powder. The SF powder was dissolved in hexafluoroisopropanol (HFIP, 7 wt %) with sustained stirring overnight. The resultant SF/HFIP was cast on the glass plate in a chamber to avoid fast evaporation. After air-drying, the resulting SFms were subjected to insoluble processing and rinsing until HFIP was removed.

2.2. Testing of Affinity Binding of HL to SFm and Pro-osteogenesis Ability of HL. To simulate the binding between HL and SF, we employed the fibroin N-terminal domain (fibNT) to represent SF, using a protein databank (PDB) identification of 3UA0.[23] Because short peptides lack 3D structures, the peptide–protein complex was generated using the online HDOCK web

https://doi.org/10.1021/acsami.2c17554
ACS Appl. Mater. Interfaces 2023, 15, 7673−7685

server.[24,25] After the PDB file was uploaded as a receptor molecule and the peptides were treated as a ligand molecule, the docking results were visualized and analyzed in 3D.

The BMP-2 core sequence peptide (KL) and bi-functional peptide (HL) were obtained by commercial synthesis (>95% purity, GL Biochem Ltd., China). KL and HL were both labeled with fluorescein isothiocyanate (FITC), forming KL-F and HL-F, respectively, for the binding-elution test. These lyophilized peptides were dissolved in deionized water to prepare an aqueous stock solution. SF membranes were incubated with an equimolar concentration (10 μM) of FITC, KL-F, or HL-F for 2 h. The uncombined remnants were removed thoroughly. Confocal laser scanning microscopy (CLSM) was used to capture the remaining fluorescence signals excited from SF membrane-bound peptides. The semiquantitative analysis of mean fluorescence intensity was calculated using Image J software.

To quantify the difference in binding force between HL and KL, we conducted adsorption tests. The surface functionalization of SFm with peptides was carried out by previously reported methods with small modifications.[26] HL or KL (0.1 μM) was incubated with the SF films cast in a 24-well plate for 2 h at 37 °C. Then the films were rinsed and the eluent was collected with the supernatant to calculate the percentage of peptides remaining on the SF surface, which was defined as functionalization efficiency.

The pro-osteogenic differentiation function of HL was checked by osteocalcin (OCN) expression of MSCs. We added KL and HL in the same molar amount (400 μmol) per well in a 12-well plate for the test with the group of no peptide as the negative control and the group with double amount of KL (800 μmol) as the positive control. KL and HL were pre-coated on the bottom surface of the wells and then sterilized before cell seeding. MSCs were then cultured on the peptide coatings in a quantity of $2 \times 10^4/cm^2$ for 3 d without a change of the culture medium. The total RNA of MSCs was collected and reverse-transcribed into complementary DNA (cDNA). The cDNA was amplified by PCR and the products then were subjected to agarose gel electrophoresis to measure mRNA expression levels of OCN. GAPDH levels are shown as a comparison.

2.3. Self-Assembling Properties of the Peptides. The lyophilized powders of the peptide were dissolved in deionized water in 1 mg/mL aliquot of stock. Transmission electron microscopy (TEM) and atomic force microscope (AFM) were used to observe the self-assembly behaviors of synthetic peptides. The peptides were diluted with deionized water before imaging. Then, 5 μL of the peptide solution was dropped on a copper grid for TEM characterizations. After air-drying, the uranium acetate solution was dropped on the copper grid to distinguish the peptides' contour by negative staining and the extra solution was then removed with filter paper. For AFM observation in tapping mode, a newly stripped mica sheet was used to support the sample.

2.4. Characterization of Peptide-bonded SF Membranes. To modify the SF membranes, we adopted a layer-by-layer incubation strategy. Briefly, KL and HL peptide solutions were added to well plates with SF membranes. After 1 h of co-incubation with gentle shaking, the residual solution was aspirated. PBS was used to wash the unbound peptide away from the membranes, which were then removed and air-dried. These binding−rinsing−drying steps were repeated 3 times, obtaining the peptide-modified membranes, the KL-functionalized SFm (KL@SFm) and HL-functionalized SFm (HL@SFm). Before cell experiments, the SF membranes before and after binding KL and HL were all sterilized by immersing in 70% ethanol over 10 min.

AFM in tapping mode was applied to image the modified SF membranes. The cast membranes were randomly taped on the glass in a 20×20 μm^2 area. Then 5×5 μm^2 area was zoomed in to amplify the 3D structures. The analysis of images was refined by comparing the values of root-mean-square (RMS) roughness and z-range. The contact angle of the peptide-modified SF membranes was used to estimate the surface hydrophilicity.

2.5. Cell Viability Assay and Morphology on HL@SFm. Purchased primary human MSCs (Cyagen, China) were cultured in a 5% CO_2 and 37 °C environment and passaged until the 5th generation for all cell-related experiments. Only a basic medium with 10% fetal bovine serum and 1% penicillin−streptomycin was used for the whole culturing process including the differentiation stage.

The proliferation of MSCs seeded on peptide-modified SF membranes was detected using a cell counting kit-8 (CCK-8) (Donjindo, Japan). The experimental procedures followed the standard protocol of the kit on 1, 3, and 5 d. Blank wells with the medium and 10% CCK-8 were used for subtracting the background. Finally, the incubated solution was detected at 450 nm wavelength. The cytocompatibility of the functionalized SFm was also evaluated using the live/dead assay. Following the CCK-8 test, the Calcein-AM kit was used to stain the rest of the replications in every group. Calcein-AM (1 μM) incubated with the live cells was cleaved to show green florescence. PI (2 μM) intercalated to DNA of dead cells showed red fluorescence. After immersing in a staining solution for 20 min at 37 °C, the cell samples were rinsed completely and imaged under a fluorescence microscope (excitation = 490 nm, emission = 520 nm).

To observe the cell morphology on the SF membrane surface, cell samples at each time point were fixed first and permeated by 0.1% Triton X-100. Then, they were blocked by 1% bovine serum albumin to prevent unspecific binding. The cytoskeleton of MSCs was finally stained with green-fluorescent dye conjugated to phalloidin. The extra dye solution was discarded completely and the cell images were captured under a CLSM.

2.6. Osteogenic Differentiation of MSCs on HL@SFm. For quantifying alkaline phosphatase (ALP) secretion, MSCs at 7 and 14 d were lysed by the RIPA lysis buffer with 1mM PMSF and centrifuged to obtain the supernatant. The ALP assay kit (Beyotime, China) was used to detect p-nitrophenol in the supernatant. The final enzymatic activity was normalized to total protein in cells. To directly observe the ALP expression from the cells, the color reaction kit (BCIP/NBT, Beyotime, China) was used to show the staining. After 2 weeks, MSCs were rinsed and fixed with 95% ethanol. The working staining solution was added to cover all cells for 40 min at room temperature until the color turned dark.

MSCs were harvested after cultured for 14 d. Immunofluorescent staining for collagen I (COL-I) and osteopontin (OPN) was performed using their corresponding antibodies (ab34710 and ab8448, 1:1000), and then coupled with the Alexa Fluor 555 labeled secondary antibody (1:500, Beyotime, China). The cells were nuclear stained with DAPI prior to imaging. Their mRNA levels for osteogenic-specific genes of MSCs cultured on SFm, KL@SFm, and HL@SFm were also assessed using real-time PCR. cDNA of cultured cells was obtained as mentioned in section 2.2. Specific template DNA with related primers (listed in Table S1) was amplified in 40 cycles and tested by the SYBR Green I (TAKARA, Japan) signal. The results were calculated using the $2^{-\Delta\Delta Ct}$ method using CFX Manager software (Bio-rad). The expression level was normalized by the GAPDH value. We calculated the relative expression compared with the SFm group.

2.7. *In Vivo* Ectopic Osteogenesis Model. Twenty Sprague-Dawley (SD) rats (≈200 g) were given implanting operations to evaluate the ectopic bone formation ability and histocompatibility of the SF membranes with peptides. The MSCs were only cultured on HL@SFm for 5 d in advance in a normal medium for promoting the growth of MSCs. The subcutaneous model was built as previously described[27] with minor changes. In brief, rats were anesthetized slightly by inhaling 4% isoflurane/oxygen and kept in light narcosis with 2% concentration by an anesthesia machine (ZS Dichuang Co. LTD, China). The materials were subcutaneously implanted into incisions on the back randomly and then the wound was sutured with iodophor disinfection. Subsequently, all rats received intramuscular injections of penicillin (1 mL kg^{-1}) for three consecutive days to avoid infection. Animals were sacrificed by intraperitoneal injection of an overdose of pentobarbital sodium after 4 and 8 weeks.

2.7.1. Micro-Computed Tomography (Micro-CT) Analysis of Calcified Implants. Eight weeks post-SF membrane implantation, rats were anesthetized and placed on the examination stage at a prone position. The implants' lower back region was first magnified in the

https://doi.org/10.1021/acsami.2c17554
ACS Appl. Mater. Interfaces 2023, 15, 7673−7685

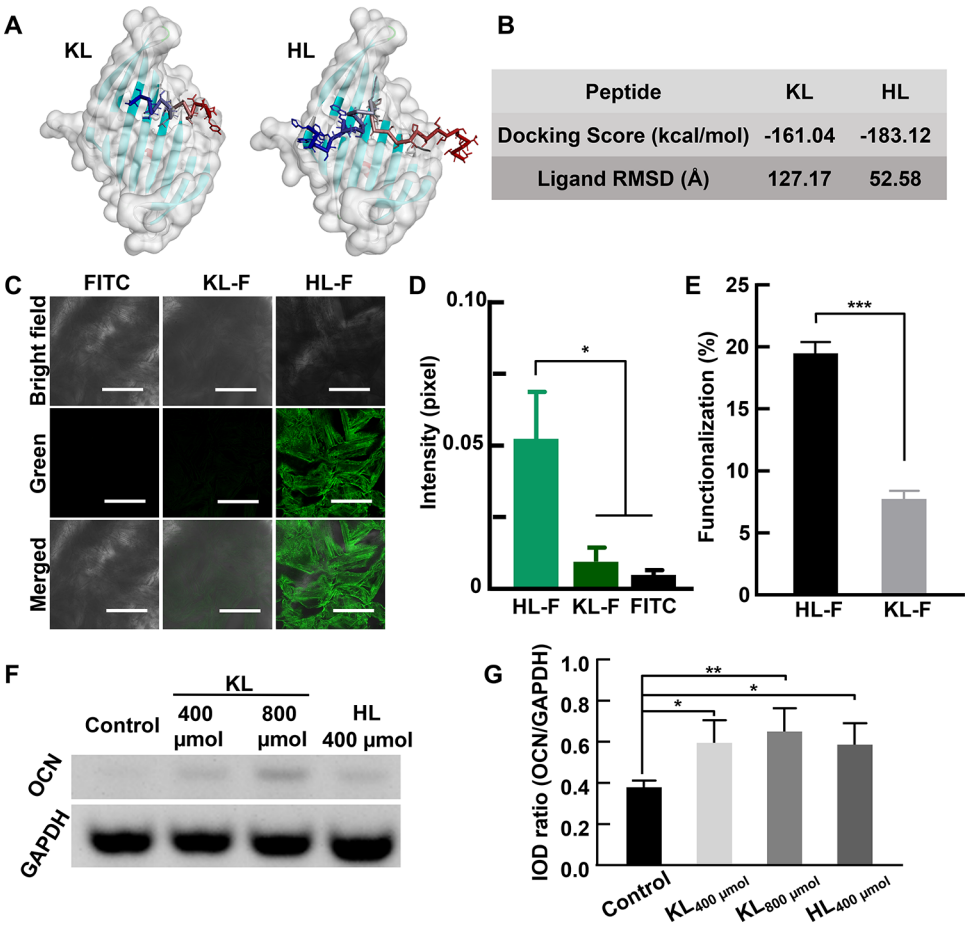

Figure 1. Functional verification of bi-functional peptides. (A) Molecular docking complex of the KL peptide or HL peptide (in rainbow colors) with highly conserved N-terminal domain of the SF heavy chain (blue secondary structure with a gray surface, PDB ID: 3UA0) obtained using the HDOCK web server. (B) Docking score and ligand RMSD of simulation models. (C) Imaging of the FITC-labeled peptides for confirming their binding to SF membranes by CLSM. (D) Semi-quantitative analysis of fluorescence intensity from CLSM images in C (Scale bar: 5 μm). (E) The adsorption analysis of HL and KL on SF films. (F) The expression of osteocalcin mRNA in MSCs cultured for 3 days under the effect of peptides and corresponding (G) semiquantitative calculation. (*$P < 0.05$, **$P < 0.01$, ***$P < 0.001$).

ultra-focus form and scanned in accurate mode (Milabs, Netherlands). After live imaging was completed, the rats were sacrificed to extract implants for rescanning individually. The obtained data were reconstructed for 3D analysis using MILabs Rec 10.16, and the total volume (TV) and bone volume fraction (BV/TV) of calcified tissue were calculated using IMALYTICS Preclinical 2.1 software. The signal display range of the images was unified with the maximum and minimum values fixed.

2.7.2. Histological and Immunohistochemical (IHC) Evaluation of Osteogenesis. All implanted SF samples and surrounding tissues were surgically extracted and immersed in 10% neutral formalin overnight for processing sections. Masson's trichrome as well as hematoxylin and eosin (H&E) were used to stain the 5-micron-thick tissue sections to analyze histological structures. To examine inflammatory responses at the site of material implantation, we further marked the distribution and expression of the proinflammatory factor interleukin-6 (IL-6) and anti-inflammatory factor interleukin-10 (IL-10) by IHC staining to evaluate their biocompatibility. The prepared sections were incubated with the primary antibody of CD31 to evaluate the formation of blood vessels. Based on the analysis of angiogenesis, the same IHC method was used to color bone-related proteins including OPN, COL-I, and OCN to check the expression difference of bone matrixes around implantation areas. The slices obtained above were scanned into full-piece images. And all IHC staining results were compared semi-quantitatively with respect to the integrated optical density (IOD) processed by Image J software.

All surgical operations of animal testing were approved by the Animal Ethics Committee of Zhejiang University following the Guidelines for Care and Use of Laboratory Animals of Zhejiang University.

2.8. Statistical Analysis. All these data were in the form of mean ± standard deviation. Group differences were analyzed by One-way ANOVA calculation with Prism version 9.0 (GraphPad) and accepted as statistically significant when *$P < 0.05$, **$P < 0.01$, ***$P < 0.001$. If the P value is greater than 0.05, the results are considered to show no statistical difference.

3. RESULTS AND DISCUSSION

3.1. Computational Simulation of Peptide−Protein Docking. In the research of SF biomaterial, the study of SF was always focused on the heavy chain or light chain/heavy chain mixture of SF.[28] Heavy chain comprises a highly conserved N-terminal hydrophilic domain (fibNT, PDB: 3UA0), which can be used as SF to reveal the binding sites.[23] As the docking models exhibited (Figure 1A), the HL peptide was more preferentially binding to the stable β-sheet area of fibNT and had more residue pairs (distances < 5.0 Å) with fibNT than KL did (Table S2). In general, the lower the RMSD value obtained from the re-docking experiment, the better the docking pose for the binding mode of the ligand.[19] The same goes for the docking score. The HL peptide had a

https://doi.org/10.1021/acsami.2c17554
ACS Appl. Mater. Interfaces 2023, 15, 7673−7685

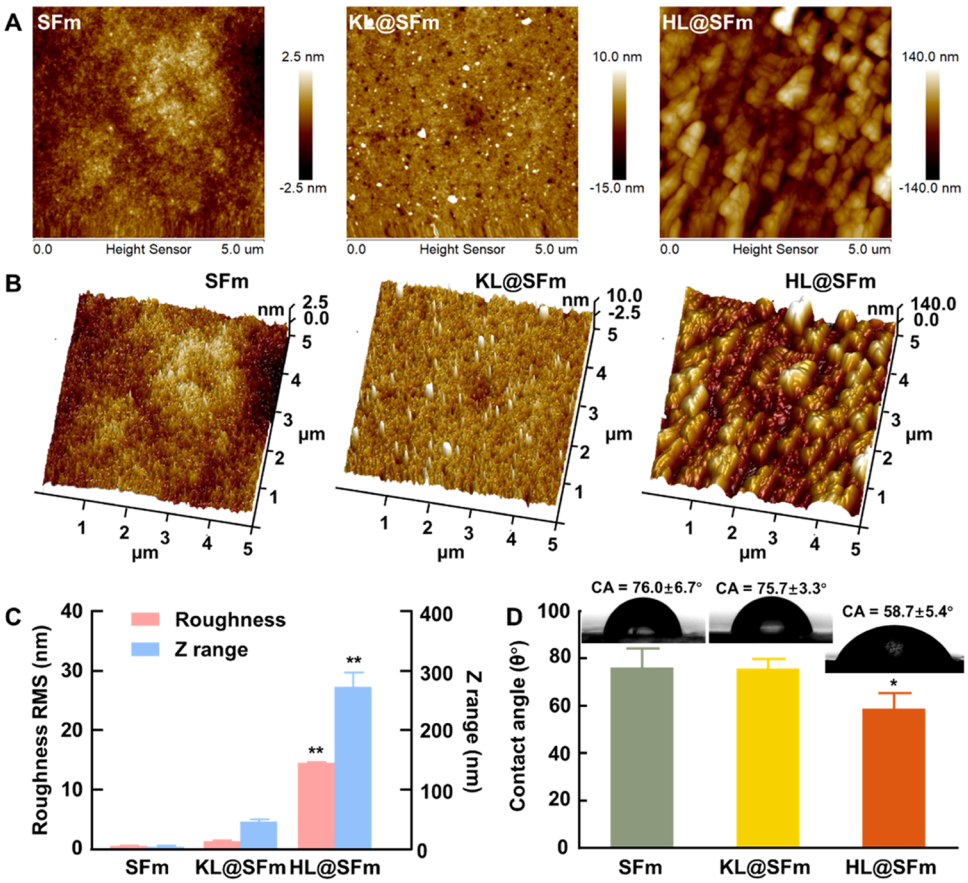

Figure 2. Morphologies and hydrophilicity of modified SFm. (A) 2D topographies and (B) corresponding 3D structures of SFm, KL@SFm, and HL@SFm surfaces. (C) Semi-quantitative analysis of root-mean-square (RMS) roughness and *z*-range from AFM images. (D) Water contact angle measurements. Statistical significance only showed the difference between HL@SFm with other groups (*$P < 0.05$, **$P < 0.01$).

better simulation docking posing based on the lower binding energy than the KL peptide (Figure 1B). Therefore, the heavy chain domain of SF used in the peptide−protein binding simulation represents that HL has a better binding affinity with SF than KL.

3.2. Functional Verification and Self-Assembling Properties of Bi-Functional Peptides. To further confirm the binding affinity of the peptides to SFm, we conducted the binding-elution test of HL with SFm in comparison with two other groups (free FITC and KL). As shown in CLSM images (Figure 1C), stronger green fluorescence could be seen in the HL group than in the other groups. Semi-quantitative intensity statistics also showed that the fluorescence of the HL group was typically higher than that of the other two groups (Figure 1D), indicating that HL can tightly bind to the SF material even after multiple prolonged washes. Additionally, the adsorption assay (Figure 1E) showed the detailed efficiency of functionalized HL (19.47%) and KL (7.66%) calculated by the standard curves of fluorescent peptides (Figure S2). This result indicates that HL could bind to the SF surface to significantly functionalize the surface with a greater ability than KL.

Next, we verified the osteogenic function of HL to demonstrate that the KL motif in HL still retains its biological functions (Figure 1F,G). In contrast to the blank control, HL induced the OCN expression at a level similar to the equimolar KL. A higher KL amount (800 μmol) indeed induced more OCN expression. We made the HT sequence retain an active N-terminus and link it with the KL part by the Gly-Gly-Gly-Gly linker. An appropriate linker can establish steric hindrance to maximizing the binding efficiency of the protruding peptide motif.[29] Collectively, the above results proved that HL retained two independent functions, the SF-binding by the HT motif and the osteogenic capability by the KL motif, laying the foundation for the use of the HL-modified SFm (HL@SFm) in bone regeneration.

Additionally, we observed the self-assembly morphologies of peptides by both TEM and AFM (Figure S3). KL and HL peptides exhibited different self-assembly behaviors in the aqueous solution. KL had short rod-like structures with a length of about 2−3 μm, while HL formed tightly packed particle-like structures. Through these observations, it can be confirmed that different functional peptides can trigger self-assembly behavior in the aqueous solution. Combined with the results of functional verification tests, it was also proven that the embedding of two sequences with different functions did not affect the function of the two motifs. The self-assembly may also affect the modification of the SF surface morphology by the peptides.

3.3. Surface Modification of SFm from Anchored HL. AFM images revealed significant differences in the topographies of the SF surfaces modified with different peptides (Figure 2A,B). The surface of SFm was flat and smooth. After co-incubation with the KL peptide, a few scattered dot-like deposits appeared on the resultant KL@SFm surface. Due to the lack of the SF-binding ability, most of the KL peptides were

https://doi.org/10.1021/acsami.2c17554
ACS Appl. Mater. Interfaces 2023, 15, 7673−7685

eluted during washing and drying, resulting in sparse deposits on KL@SFm. The HL@SFm consisted of highly homogeneous nanoparticles (about 200−300 nm in size) stacked up to form a large piece of a dot-to-plane topography. The 3D images of different membranes exhibited a distinct protrusion structure of HL@SFm, with the highest protrusion height on the *z*-axis. Quantitative analysis of the AFM images directly reflected the fact that the addition of peptides significantly improved the *z*-range of the membrane surface compared with pure SFm (Figure 2C). In particular, HL@SFm reached the maximum "*z*" value of 272.67 ± 19.57 nm while the SFm exhibited the lowest *z* value of 4.62 ± 0.91 nm. Just like the *z*-range, the RMS roughness was decreased in the order of HL@SFm (31.8 ± 1.5 nm), KL@SFm (1.30 ± 0.14 nm), and SFm (0.55 ± 0.03 nm).

The influence of peptides on the surface properties of the SFm could be another reliable evidence for SF-binding (Figure 2D). According to contact angle (CA) values, SF membranes were hydrophilic (CA < 90°). Proper hydrophilicity is advantageous for promoting cell adhesion and enhancing cell−material interactions.[30] HL@SFm, with better hydrophilicity (CA = 58.7 ± 5.4°) than KL@SFm (CA = 75.7 ± 3.3°) and SFm (CA = 76.0 ± 6.7°), could facilitate cell growth compared to KL@SFm and SFm. Additionally, the stronger SF-binding capability of HL than KL could enable HL to cover SFm more widely than KL (Figure 2B). The results of hydrophilicity and roughness of HL@SFm are consistent with the notion that the CA decreased with increasing roughness on the hydrophilic surfaces with a CA of less than 90°.[31] Collectively, the above results also demonstrate that HL@SFm presents the roughest and most hydrophilic surfaces among the three membranes.

3.4. Viability and Morphology of Cells Cultured on HL@SFm. Cytocompatibility is the principal property desired in biomedical materials. Here, we checked cell proliferation and viability as the evaluation criteria (Figure 3). The tissue culture plate (TCP) served as a control to compare the biocompatibility of SFm. There was a continuously increasing trend toward cell growth in all groups (Figure 3A). TCP, rather than SFm and KL@SFm, obviously increased the growth rate of MSCs on the first day. Then, no significant difference appeared between these groups on day 3. The good performance of TCP was due to the surface activation treatment, which facilitated cell adhesion. TCP and HL@SFm significantly improved the proliferation of MSCs on day 5 compared to the other two groups. Although the number of cells on HL@SFm was lower than that on TCP, both groups did not show any statistical difference. This may arise from the coating of the bi-functional peptide on the SFm surface with improved wettability (Figure 2D). Similarly, representative fluorescence images show high cell viability of all groups evaluated using the calcein-AM/PI kit (Figure 3B). The denser living cells represented by green fluorescence also supported the results of increasing MSC amount in the proliferation experiment. The dead cells were barely visible, especially after 3 and 5 days of culture. The rapid proliferation and high viability of cells indicated that HL@SFm had good cytocompatibility in terms of sustained maintenance *in vitro*.

In addition, from images on day 5, the majority of MSCs cultured on HL@SFm grew into a polygonal shape rather than an undifferentiated spindle-like shape. We then monitored the morphology of MSCs by staining the cytoskeleton (Figure S4). All groups were able to encourage the adhesion of MSCs.

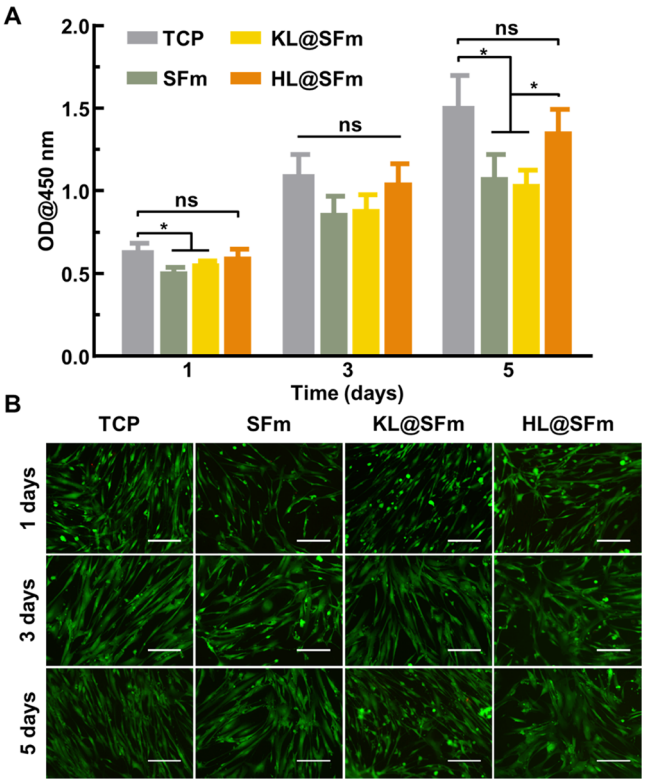

Figure 3. Time courses of MSC proliferation and live/dead staining on TCP, SFm, KL@SFm, and HL@SFm for 1, 3, and 5 days. (A) Proliferation of MSCs reflected by the OD value at 450 nm. (B) Fluorescence images of MSC viability. Live cells were labeled by calcein-AM in the green channel and the dead cells were labeled by PI on nuclei in red (Scale bar: 200 μm, $^*P < 0.05$, ns means no statistical difference).

However, the cells on the TCP, SFm, or KL@SFm remained elongated, whereas those on HL@SFm tended to be spread. Especially on days 3 and 5, in the HL@SFm group, actin bundles concentrated at the tonofilament and filopodia area, which would be helpful for cell migration and differentiation. The brightly stained actins also corresponded to a clear cytoskeleton that influenced the initiation of stem cell differentiation through the mechanical properties of tension.[32] Through the growth state of seed cells on HL@SFm, the cell support and adhesion performance of the scaffolds can be verified.

3.5. Osteogenic Differentiation of MSCs on Functionalized SF Membranes in the Absence of Osteogenic Supplements. ALP is an exoenzyme expressed by osteoblasts, and its expression activity is a significant feature of osteoblast differentiation.[33] Cells in all groups (SFm, KL@SFm, and HL@SFm) started to have the expression of ALP on day 7, and enzyme expression was enhanced after 2 weeks (Figure 4A). However, MSCs on HL@SFm showed the highest ALP activity at both time points, confirming its strongest osteogenic effect early in differentiation. We also performed the staining assays to observe the ALP distribution of MSCs on the SF surfaces (Figure 4B). Macroscopic photos displayed a larger area and deeper ALP staining in the HL@SFm group than the other two groups. In addition to staining for expressed ALP, the heavily stained cells produced more surface-contact anchors and more pseudopodia compared with the unstained spindle-shaped cells.

https://doi.org/10.1021/acsami.2c17554
ACS Appl. Mater. Interfaces 2023, 15, 7673−7685

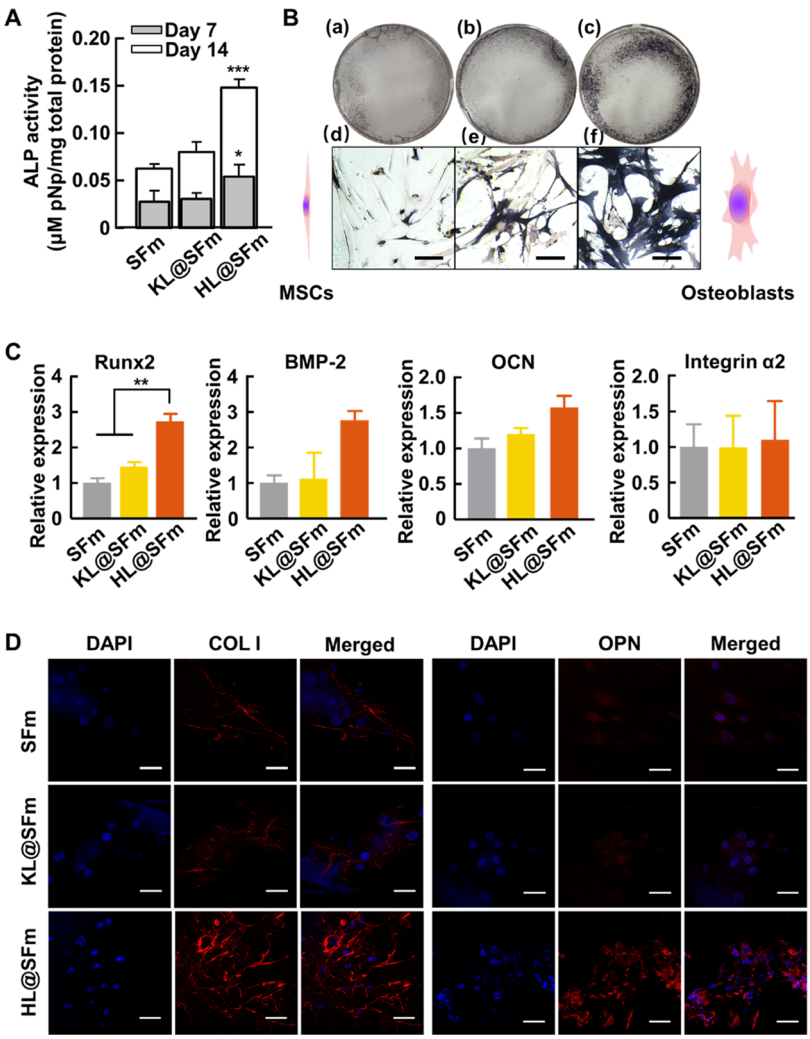

Figure 4. Bi-functional peptides on SFm promoted osteogenesis *in vitro*. (A) Relative enzymatic activity of ALP on days 7 and 14. Statistical significance only showed the difference between SFm (control group) with other groups. (B) ALP staining of MSCs in macroscopic (a−c) and microscopic (d−f) views on day 14. (C) The expression level of osteogenesis-associated genes. (D) COL-I and OPN-stained immunofluorescent images of MSCs labeled with Alexa Fluor 555 (Scale bar: 30 μm, $^{*}P < 0.05$, $^{**}P < 0.01$, $^{***}P < 0.001$).

To investigate the effect of HL@SFm on the osteogenesis of MSCs, osteogenesis-related genes, including OCN, BMP, and runt-related transcription factor 2 (Runx2) were detected. The HL@SFm group showed the highest expression levels of all three genes (Figure 4C), demonstrating its marked ability to enhance osteogenic differentiation of MSCs. In particular, HL@SFm showed a significantly higher level of expression of Runx2, a marker of osteoblast differentiation,[34] than the other two groups. Next, we stained bone-associated protein markers by immunofluorescence (Figure 4D). MSCs cultured on HL@SFm exhibited a higher level of COL-I and OPN than those on SFm and KL@SFm, indicating that HL@SFm had the strongest capacity for inducing osteogenic differentiation without the addition of other chemical inducers in the medium. Taken together, these results consistently verified that the modification of SF membranes by HL peptides provided a more suitable microenvironment for inducing the osteogenic differentiation of MSCs. This is because HL@SFm bears a combination of biophysical cues (e.g., the unique surface topography) and biochemical signals (e.g., the KL peptide motif).

3.6. *In Vivo* Bone Tissue Formation Induced by HL@SFm. Ectopic bone models are often applied to test bone formation induction by soft materials. Hence, we evaluated the osteogenic ability of HL@SFm in the subcutaneous area of rats. Quantification of the tissue volume (TV) by micro-CT revealed that HL@SFm seeded with or without MSCs had a greater volume of calcified tissue formed on the implanted SF membranes than SFm and KL@SFm (Figure 5B). Furthermore, the quantified percentage (bone volume/TV, BV/TV) showed a similar increase in the newly regenerated bone in the HL@SFm with or without MSCs groups (Figure 5C) compared to the other two groups, with the HL@SFm with MSCs showing a stronger bone induction capability than that without MSCs. Even though there was no statistical difference between HL@SFm with SFm and KL@SFm, actual *in vivo* 3D-scanning images again demonstrated that HL@SFm relatively showed the formation of a bulk of calcified tissue (Figure 5D). Little calcified tissue was observed in the SFm and KL@SFm groups in the micro-CT images. However, compared to these two groups, HL@SFm with or without seeded cells had a strong calcified signal, especially the signal intensity of the group with cells was very close to that of the nearby hip bone

https://doi.org/10.1021/acsami.2c17554
ACS Appl. Mater. Interfaces 2023, 15, 7673−7685

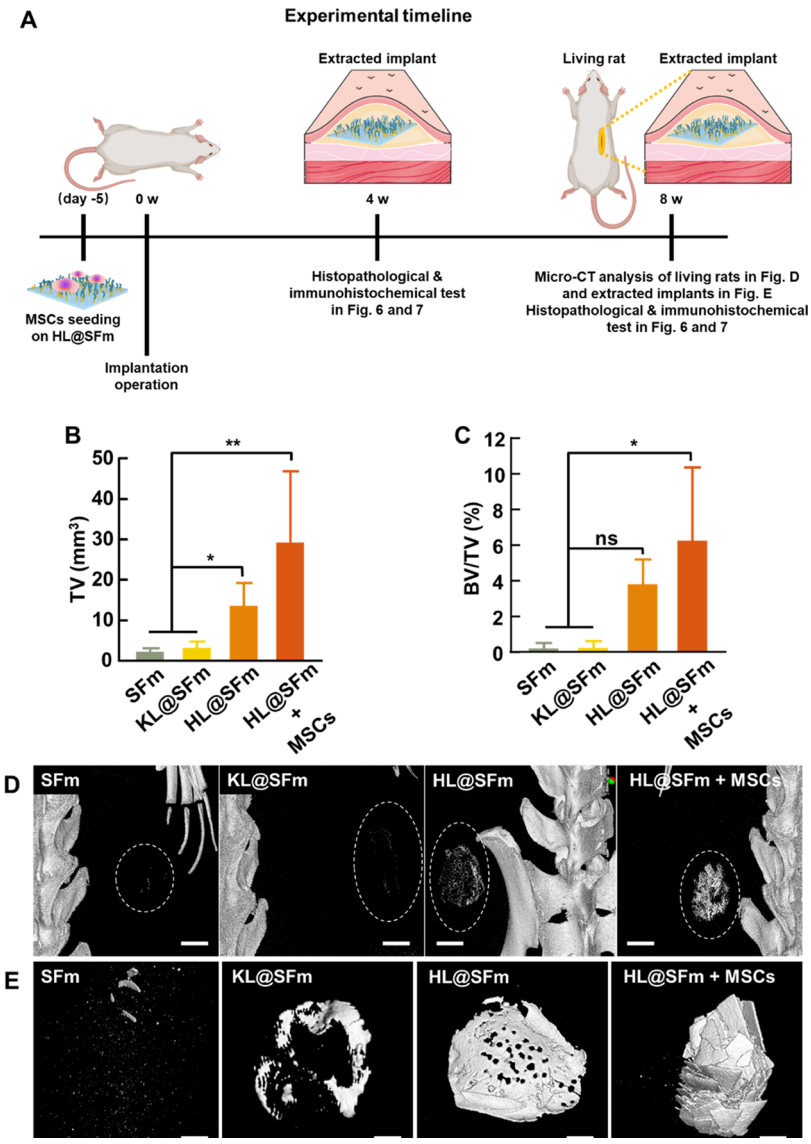

Figure 5. Evaluation of ectopic osteogenesis from implanted functional SFm by micro-CT. (A) The experimental timeline of osteogenesis assay in vivo. (B) TV and (C) BV/TV of newly formed calcified tissue determined by quantitative micro-CT analysis (*$P < 0.05$, **$P < 0.01$, ns means no statistical difference). (D) The micro-CT visualization of 3D reconstructed implant structures with the intensity of natural bone being set as a reference (Scale bar: 5 mm. The dotted ellipses show the graft's position). (E) The comparison of extracted implants *in vitro* by micro-CT imaging (Scale bar: 2 mm).

(Figure 5D). Furthermore, when the implants were taken out of the animals, their representative 3D micro-CT images (Figure 5E) showed that new mineralized tissue tended to deposit from the edge to the center of the SF membranes (SFm, KL@SFm, and HL@SFm). It was clear that the membrane structure of HL@SFm without MSCs remained relatively intact, whereas the seeding of MSCs accelerated the degradation of the HL@SFm membrane structure during bone formation (Figure 5E). Therefore, we can conclude that the HL peptide indeed induced the heterotopic ossification of implanted HL@SFm, which is thus a promising biomaterial in BTE.

3.7. Biocompatibility of Implanted SF Membranes *In Vivo*. We then evaluated the histocompatibility of HL@SFm. H&E and Masson staining (Figure 6) showed the implanted SF membrane and their surrounding fibrous tissue. A few neutrophils and phagocytes were found in the tissue around the grafts in all groups, suggesting a mild inflammatory response *in vivo* to the SF membranes with or without peptide coating. Lots of capillaries were observed around the HL@SFm groups with or without MSCs. Extending the implantation time, the HL@SFm group induced increased blood vessel formation in the fibrous tissue.

Moreover, there were more blood vessels around HL@SFm with MSCs than without MSC seeded. This phenomenon could be explained by the migration of MSCs to the implantation site, which affects the formation of new blood vessels.[35] Therefore, adding seed cells can accelerate angiogenesis in the grafts. A flood of phagocytes damaged the membrane in the group of HL@SFm with MSCs and the blood vessels also formed at the degradation site (Figure 6B), suggesting that the surrounding inflammatory cells may be involved in forming blood vessels.[36,37] Masson staining showed that dense fibrous connective tissues were formed in all groups at 4 weeks (Figure 6A). Thinner fibrous capsules were observed after 8 weeks (Figure 6B), demonstrating the relief

https://doi.org/10.1021/acsami.2c17554
ACS Appl. Mater. Interfaces 2023, 15, 7673−7685

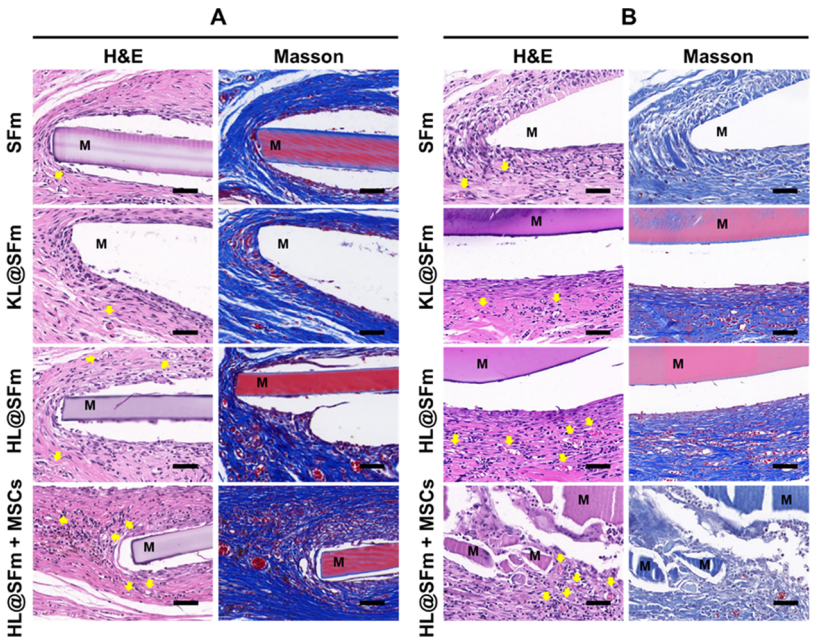

Figure 6. H&E and Masson's trichrome staining of SFm, KL@SFm, and HL@SFm with and without MSCs subcutaneously implanted in the SD rat model after (A) 4 weeks and (B) 8 weeks. The yellow arrows and letter M represent blood vessels and implanted membranes, respectively. (Scale bar: 50 μm).

of inflammatory response. In addition, the typical blue staining of fibrous COL-I was found in the HL@SFm groups with MSCs, illustrating the formation of mature collagen fibers (Figure 6A).

3.8. Immunohistochemical Analysis of HL@SFm. *3.8.1. Inflammatory Response of HL@SFm in the Implanted Environment.* We then performed immunohistochemical staining of the above implants to explore the causes of osteogenic differences. Based on the results of H&E and Masson's trichrome staining, we selected two representative inflammatory factors to be characterized. Inflammation is defined as a continuous proinflammatory and anti-inflammatory process to achieve a balanced state. IL-6 is considered a marker protein having high expression in the early stage of inflammation. As shown in Figure 7A, the tissue edges around SFm, KL@SFm, and HL@SFm showed obvious and similar brown color at 4 w, which also corresponded to the generation of mild inflammatory reactions in H&E sections. While there was no immunostaining reaction in HL@SFm+MSCs, the IOD value for this group was significantly lower than that for the HL@SFm group (Figure 7B), indicating that the infiltration of MSCs weakened the inflammatory response. After 8 w, the expression of IL-6 in all groups except the HL@SFm+MSCs decreased significantly, indicating that the inflammatory response was alleviated. But this phenomenon was more likely to be interpreted as the unique anti-inflammatory property of macrophages co-cultured with MSCs, which was the high expression of IL-6, the opposite cytokine secretion behavior of monocyte-derived proinflammatory macrophages.[38] The non-single up/down-regulation of IL-6 also showed its complex role in the proinflammatory process. Unlike the classical proinflammatory factor TNF-α, IL-6 has not produced a simple inhibitory effect on osteogenic differentiation in other studies,[39] and can even show a bone-promoting effect both *in vivo* and *in vitro*.[40] This may also promote bone formation of HL@SFm + MSCs.

As for the expression results of IL-10, all groups showed darker IL-10 staining after 4 w than the founding of 8 w. The high expression of IL-10 indicated that with an inevitable inflammatory reaction, the materials in each group were conducive to turning monocytes into macrophages with anti-inflammatory phenotypes. Thus, anti-inflammatory markers could be produced to reduce inflammation and enhance tissue repair and angiogenesis. After 8 w, the expression of IL-10 decreased, indicating that they still maintained the function and continuously suppressed inflammatory response. Overall, SF membranes were biocompatible depending on the small amount of distributed inflammatory cells and secretion of cytokines when they were transplanted *in vivo*, and could be degraded into small irregular pieces subcutaneously.

3.8.2. Pro-Angiogenic Ability of HL@SFm In Vivo. Angiogenesis is a prerequisite for bone formation. The vascularization of bone tissue engineering materials can effectively link the internal structure of bone to maintain cell viability and promote bone integration. Therefore, CD31 was selected here as the marker protein of endothelial cells to observe angiogenesis in the surrounding fibrocystic layer after 8 w. As Figure S5A shows, there were a certain number of tiny vessels with diameters of about 20−30 μm near the fibrous capsule of SFm and KL@SFm. Denser vascular lumens with larger cross-sectional areas were distributed around HL@SFm and HL@SFm+ MSCs. Especially in HL@SFm+ MSCs, vessels were also located at places where the membranes were broken into pieces, demonstrating the formation of connected vascular structures within them. Further statistics revealed that the more obvious difference in the angiogenesis capacity was the cross-section area of the vessels rather than the number of vessels (Figure S5B,C). Moreover, the area of neovascularization was more significantly elevated after MSC seeding on HL@SFm. This result suggested that the newly generated vessels around SFm and KL@SFm were small and dense and they cannot achieve efficient blood supply. However, HL@SFm and HL@SFm + MSCs generated vessels

https://doi.org/10.1021/acsami.2c17554
ACS Appl. Mater. Interfaces 2023, 15, 7673−7685

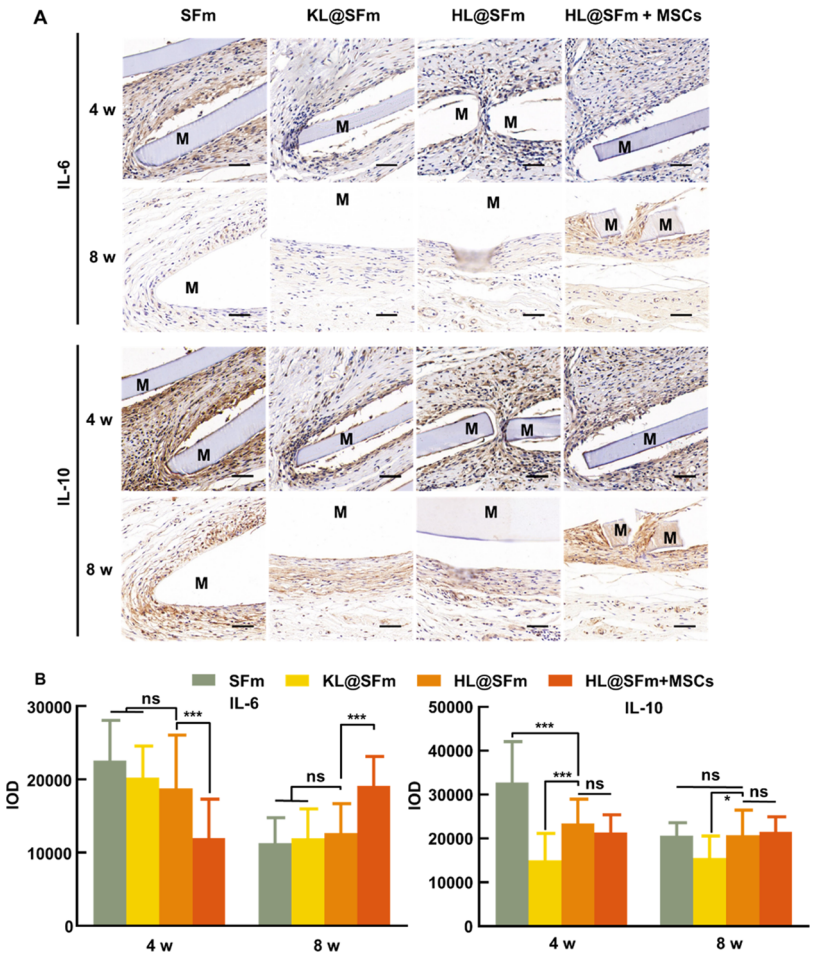

Figure 7. Local inflammatory response to the implanted membranes. (A) IHC staining of IL-6 and IL-10 and the corresponding semiquantitative results (B) in the subcutaneously implanted SFm, KL@SFm, HL@SFm, and HL@SFm + MSCs after 4 weeks and 8 weeks. Letter M represents implanted membrane position. Statistical analysis only showed the difference between HL@SFm and other groups (Scale bar: 50 μm, *P < 0.05, ***P < 0.001, ns means no statistical difference).

with both wide diameter and large amount, which facilitated the establishment and connection of the vascular network. Correlating the results of newly generated vessels with the newly formed calcified tissue also verified that well-established angiogenesis was indispensable for inducing osteogenesis.

3.8.3. Formation of Bone Matrix Proteins. Figure 8 shows that the expression of bone-related proteins increased with increasing transplantation time. At 4 weeks, OPN staining displayed a positive expression among all the groups, whereas COL-I and OCN staining only showed a positive expression in the HL@SFm with the MSCs group (Figure 8A). The semiquantitative analysis showed a significant increase from HL@SFm with and without MSCs than SFm and KL@SFm (Figure 8C). The possible reason is the multi-role of OPN in osteogenesis. In addition to being related to cell adhesion and bone matrix formation, OPN is also associated with high expression influenced by infiltrating white blood cells or other macrophages near the wound during the acute inflammatory period.[41] Therefore, it may also cause the obvious positive staining of SFm and KL@SFm at the early stage (4 w) even without other bone protein expression. Although the COL-I expression level of HL@SFm was significantly lower than that of HL@SFm+MSCs at 4 w, it was remarkably increased at 8 w with obvious brown distribution around the membrane (Figure 8A), close to the degree of the HL@SFm+MSCs group. *In vivo*, osteoblasts secrete a large amount of COL-I into ECM during the differentiation stage, interacting with various osteocytes and allowing the deposition of hydroxyapatite crystals for the formation of a mature bone.[42] OCN is also an important bone matrix protein, reflecting the maturity of bone formation. Compared with COL-I and OPN, OCN secretion is more representative as a biochemical marker of bone formation. It can be clearly observed in Figure 8A that only brown deposition of OCN appeared around HL@SFm + MSCs. The expression level was significantly higher than that of the rest of the three groups. On prolonging the implantation time to 8 w, OCN expression in all groups significantly increased. Especially the IOD value of HL@SFm achieved an order-of-magnitude increase, which was significantly higher than that of SFm and KL@SFm groups. However, it still did not reach the effect of HL@SFm + MSCs, indicating that the existence of MSCs promoted OCN expression.

The above staining results suggested that HL@SFm with the bi-functional HL peptide facilitated the bone matrix protein expression at the ectopic bone site with the increasing implantation time. In conclusion, due to the combination of seed cells (MSCs), SF scaffolds (SFm), and osteogenic signals (KL motif in HL), the HL@SFm has an excellent osteogenic effect in vivo.

https://doi.org/10.1021/acsami.2c17554
ACS Appl. Mater. Interfaces 2023, 15, 7673−7685

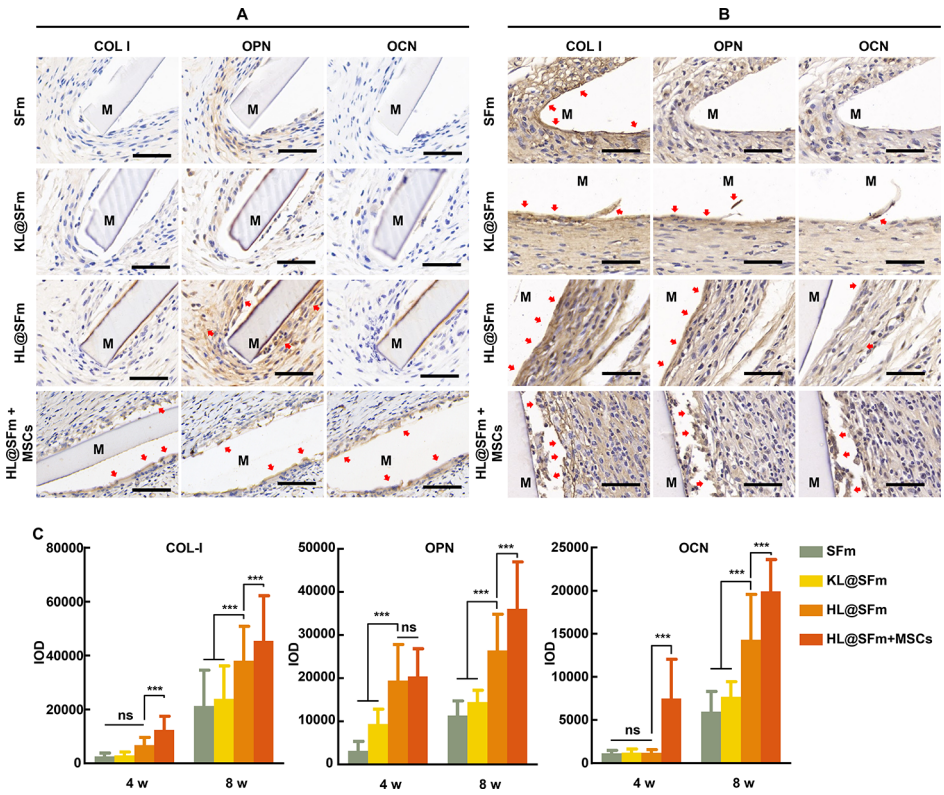

Figure 8. The expression of OPN, OCN, and COL-I in subcutaneously implanted SFm, KL@SFm, and HL@SFm with or without MSCs after (A) 4 weeks and (B) 8 weeks. Red arrows indicated positive protein deposition. Letter M represents implanted membranes. (C) Semi-quantitative analysis of IHC results (Scale bar: 50 μm, ***$P < 0.001$, ns means no statistical difference).

4. CONCLUSIONS

In summary, we have designed a novel bi-functional peptide HL, made of an SF-binding motif (HT) and an osteogenic BMP-2-derived peptide motif (KL), to modify the SF membrane to induce not only the osteogenic differentiation of MSCs without additional inducers but also the formation of the bone matrix *in vivo*. The HT motif enabled the HL to bind to SFm during a layer-by-layer process, forming HL@SFm. The docking simulation confirmed that HL could bind SF tightly due to the presence of the HT motif. Meanwhile, the KL motif in the HL sequence inherited the biological activity of BMP-2 to induce osteogenic differentiation of MSCs. The modification of SFm by HL improved the hydrophilicity of SFm and facilitated cell attachment and growth, and formed a unique topography on the SFm. We also confirmed that the HL@SFm effectively promoted the secretion of early osteogenic markers and the expression of bone-related genes and proteins. Moreover, the subcutaneous ectopic osteogenesis experiments showed that the HL@SFm could form calcified osteoid tissue with good biocompatibility even without cell seeding. In summary, this work demonstrates that the specific bi-functional peptide can be well bound on the SF matrix, forming a biomaterial that can be applied to bone tissue regeneration. Notably, this study provides an experimental basis for the safe and effective modification of biomaterials by biopanning-derived peptides.

■ ASSOCIATED CONTENT

Supporting Information

The Supporting Information is available free of charge at https://pubs.acs.org/doi/10.1021/acsami.2c17554.

Origins for realizing peptide binding with the SF substrate and growth factor selection (Figure S1); standard curves of KL-F and HL-F in aqueous solution (Figure S2); self-assembled structures of KL and HL peptides in aqueous solution under AFM and TEM observation (Figure S3); morphology of MSCs on TCP, SFm, KL@SFm, and HL@SFm with F-actin stained in green after the cells were cultured for 1, 3, and 5 days (Figure S4); angiogenic analysis of IHC staining of CD31 in subcutaneously implanted SFm, KL@SFm, HL@SFm, and HL@SFm + MSCs after 8 w (Figure S5); primer sequences used for gene expression analysis (Table S1); receptor−ligand interface residue pairs of KL and HL with fibNT (Table S2) (PDF)

■ AUTHOR INFORMATION

Corresponding Authors

Chuanbin Mao − *School of Materials Science & Engineering, Zhejiang University, Hangzhou, Zhejiang 310058, P. R. China;* orcid.org/0000-0002-8142-3659; Email: maophage@gmail.com

Mingying Yang − *Key Laboratory of Silkworm and Bee Resource Utilization and Innovation of Zhejiang Province, Institute of Applied Bioresource Research, College of Animal Science, Zhejiang University, Hangzhou, Zhejiang 310058, P. R. China;* orcid.org/0000-0003-1256-6514; Email: yangm@zju.edu.cn

Authors

Ruyin Lyu − *Key Laboratory of Silkworm and Bee Resource Utilization and Innovation of Zhejiang Province, Institute of Applied Bioresource Research, College of Animal Science,*

Zhejiang University, Hangzhou, Zhejiang 310058, P. R. China

Yuping Chen − *Key Laboratory of Silkworm and Bee Resource Utilization and Innovation of Zhejiang Province, Institute of Applied Bioresource Research, College of Animal Science, Zhejiang University, Hangzhou, Zhejiang 310058, P. R. China*

Yajun Shuai − *Key Laboratory of Silkworm and Bee Resource Utilization and Innovation of Zhejiang Province, Institute of Applied Bioresource Research, College of Animal Science, Zhejiang University, Hangzhou, Zhejiang 310058, P. R. China;* orcid.org/0000-0003-3313-1800

Jie Wang − *Key Laboratory of Silkworm and Bee Resource Utilization and Innovation of Zhejiang Province, Institute of Applied Bioresource Research, College of Animal Science, Zhejiang University, Hangzhou, Zhejiang 310058, P. R. China;* orcid.org/0000-0002-4677-4891

Leihao Lu − *Key Laboratory of Silkworm and Bee Resource Utilization and Innovation of Zhejiang Province, Institute of Applied Bioresource Research, College of Animal Science, Zhejiang University, Hangzhou, Zhejiang 310058, P. R. China*

Qichao Cheng − *Key Laboratory of Silkworm and Bee Resource Utilization and Innovation of Zhejiang Province, Institute of Applied Bioresource Research, College of Animal Science, Zhejiang University, Hangzhou, Zhejiang 310058, P. R. China*

Jiangfeng Cai − *Key Laboratory of Silkworm and Bee Resource Utilization and Innovation of Zhejiang Province, Institute of Applied Bioresource Research, College of Animal Science, Zhejiang University, Hangzhou, Zhejiang 310058, P. R. China*

Complete contact information is available at: https://pubs.acs.org/10.1021/acsami.2c17554

Notes

The authors declare no competing financial interest.

■ ACKNOWLEDGMENTS

We acknowledge the support from the National Natural Science Foundation of China (81871499, 31800807, and 81871482), the Zhejiang Provincial Natural Science Foundation of China (LZ17C170002, LY22E030004), the National Postdoctoral Science Foundation of China (2018M632483, 2019T120519), the Fundamental Research Funds for the Central Universities (2018XZZX001-11), the State of Sericulture Industry Technology System (CARS-18-ZJ0501), and the Zhejiang Provincial Science and Technology Plans (2016C02054-19).

■ REFERENCES

(1) Andreev, D.; Liu, M.; Weidner, D.; Kachler, K.; Faas, M.; Grüneboom, A.; Schlötzer-Schrehardt, U.; Muñoz, L. E.; Steffen, U.; Grötsch, B.; Killy, B.; Krönke, G.; Luebke, A. M.; Niemeier, A.; Wehrhan, F.; Lang, R.; Schett, G.; Bozec, A. Osteocyte Necrosis Triggers Osteoclast-Mediated Bone Loss through Macrophage-Inducible C-Type Lectin. *J. Clin. Invest.* **2020**, *130*, 4811−4830.

(2) Caplan, A. I. Adult Mesenchymal Stem Cells for Tissue Engineering versus Regenerative Medicine. *J. Cell. Physiol.* **2007**, *213*, 341−347.

(3) Wang, J.; Yang, M.; Zhu, Y.; Wang, L.; Tomsia, A. P.; Mao, C. Phage Nanofibers Induce Vascularized Osteogenesis in 3D Printed Bone Scaffolds. *Adv. Mater.* **2014**, *26*, 4961−4966.

(4) Wang, Y.; Kim, H.-J.; Vunjak-Novakovic, G.; Kaplan, D. L. Stem Cell-Based Tissue Engineering with Silk Biomaterials. *Biomaterials* **2006**, *27*, 6064−6082.

(5) Bose, S.; Roy, M.; Bandyopadhyay, A. Recent Advances in Bone Tissue Engineering Scaffolds. *Trends Biotechnol.* **2012**, *30*, 546−554.

(6) Zhao, D.; Zhu, T.; Li, J.; Cui, L.; Zhang, Z.; Zhuang, X.; Ding, J. Poly(Lactic-Co-Glycolic Acid)-Based Composite Bone-Substitute Materials. *Bioact. Mater.* **2021**, *6*, 346−360.

(7) Rockwood, D. N.; Preda, R. C.; Yücel, T.; Wang, X.; Lovett, M. L.; Kaplan, D. L. Materials Fabrication from Bombyx Mori Silk Fibroin. *Nat. Protoc.* **2011**, *6*, 1612−1631.

(8) Saleem, M.; Rasheed, S.; Yougen, C. Silk Fibroin/Hydroxyapatite Scaffold: A Highly Compatible Material for Bone Regeneration. *Sci. Technol. Adv. Mater.* **2020**, *21*, 242−266.

(9) Neubauer, V. J.; Döbl, A.; Scheibel, T. Silk-Based Materials for Hard Tissue Engineering. *Materials* **2021**, *14*, 674.

(10) Karageorgiou, V.; Meinel, L.; Hofmann, S.; Malhotra, A.; Volloch, V.; Kaplan, D. Bone Morphogenetic Protein-2 Decorated Silk Fibroin Films Induce Osteogenic Differentiation of Human Bone Marrow Stromal Cells. *J. Biomed. Mater. Res.* **2004**, *71A*, 528−537.

(11) Karageorgiou, V.; Tomkins, M.; Fajardo, R.; Meinel, L.; Snyder, B.; Wade, K.; Chen, J.; Vunjak-Novakovic, G.; Kaplan, D. L. Porous Silk Fibroin 3-D Scaffolds for Delivery of Bone Morphogenetic Protein-2in Vitro Andin Vivo. *J. Biomed. Mater. Res. A* **2006**, *78A*, 324−334.

(12) Saito, A.; Suzuki, Y.; Ogata, S. I.; Ohtsuki, C.; Tanihara, M. Activation of Osteo-Progenitor Cells by a Novel Synthetic Peptide Derived from the Bone Morphogenetic Protein-2 Knuckle Epitope. *Biochim. Biophys. Acta - Proteins Proteomics* **2003**, *1651*, 60−67.

(13) Saito, A.; Suzuki, Y.; Ogata, S. I.; Ohtsuki, C.; Tanihara, M. Prolonged Ectopic Calcification Induced by BMP-2-Derived Synthetic Peptide. *J. Biomed. Mater. Res.* **2004**, *70A*, 115−121.

(14) Luo, J.; Zhang, H.; zhu, J.; Cui, X.; Gao, J.; Wang, X.; Xiong, J. 3-D Mineralized Silk Fibroin/Polycaprolactone Composite Scaffold Modified with Polyglutamate Conjugated with BMP-2 Peptide for Bone Tissue Engineering. *Colloids Surf. B Biointerfaces* **2018**, *163*, 369−378.

(15) Zheng, L.; Li, D.; Wang, W.; Zhang, Q.; Zhou, X.; Liu, D.; Zhang, J.; You, Z.; Zhang, J.; He, C. Bilayered Scaffold Prepared from a Kartogenin-Loaded Hydrogel and BMP-2-Derived Peptide-Loaded Porous Nanofibrous Scaffold for Osteochondral Defect Repair. *ACS Biomater. Sci. Eng.* **2019**, *5*, 4564−4573.

(16) Wu, J.; Zheng, A.; Liu, Y.; Jiao, D.; Zeng, D.; Wang, X.; Cao, L.; Jiang, X. Enhanced Bone Regeneration of the Silk Fibroin Electrospun Scaffolds through the Modification of the Graphene Oxide Functionalized by BMP-2 Peptide. *Int. J. Nanomedicine* **2019**, *14*, 733−751.

(17) Bilem, I.; Chevallier, P.; Plawinski, L.; Sone, E. D.; Durrieu, M. C.; Laroche, G. RGD and BMP-2 Mimetic Peptide Crosstalk Enhances Osteogenic Commitment of Human Bone Marrow Stem Cells. *Acta Biomater.* **2016**, *36*, 132−142.

(18) Wang, M.; Yang, T.; Bao, Q.; Yang, M.; Mao, C. Binding Peptide-Promoted Biofunctionalization of Graphene Paper with Hydroxyapatite for Stimulating Osteogenic Differentiation of Mesenchymal Stem Cells. *ACS Appl. Mater. Interfaces* **2022**, *14*, 350−360.

(19) Li, Y.; Qu, X.; Cao, B.; Yang, T.; Bao, Q.; Yue, H.; Zhang, L.; Zhang, G.; Wang, L.; Qiu, P.; Zhou, N.; Yang, M.; Mao, C. Selectively Suppressing Tumor Angiogenesis for Targeted Breast Cancer Therapy by Genetically Engineered Phage. *Adv. Mater.* **2020**, *32*, No. 2001260.

(20) Liu, X.; Yang, M.; Lei, F.; Wang, Y.; Yang, M.; Mao, C. Highly Effective Stroke Therapy Enabled by Genetically Engineered Viral Nanofibers. *Adv. Mater.* **2022**, *34*, No. 2201210.

(21) Zheng, S.; Lei, F.; Zhang, Q.; Mao, C.; Yang, M. Screening and Verification of Affinity Peptide for Silkworm Fibroin. *Sci. Seric.* **2019**, *45*, 0415−0420.

(22) Manchineella, S.; Thrivikraman, G.; Khanum, K. K.; Ramamurthy, P. C.; Basu, B.; Govindaraju, T. Pigmented Silk

Nanofibrous Composite for Skeletal Muscle Tissue Engineering. *Adv. Healthcare Mater.* **2016**, *5*, 1222−1232.
(23) He, Y. X.; Zhang, N. N.; Li, W. F.; Jia, N.; Chen, B. Y.; Zhou, K.; Zhang, J.; Chen, Y.; Zhou, C. Z. N-Terminal Domain of Bombyx Mori Fibroin Mediates the Assembly of Silk in Response to PH Decrease. *J. Mol. Biol.* **2012**, *418*, 197−207.
(24) Remmert, M.; Biegert, A.; Hauser, A.; Söding, J. HHblits: Lightning-Fast Iterative Protein Sequence Searching by HMM-HMM Alignment. *Nat. Methods* **2012**, *9*, 173−175.
(25) Yan, Y.; Tao, H.; He, J.; Huang, S.-Y. The HDOCK Server for Integrated Protein−Protein Docking. *Nat. Protoc.* **2020**, *15*, 1829−1852.
(26) Manchineella, S.; Thrivikraman, G.; Basu, B.; Govindaraju, T. Surface-Functionalized Silk Fibroin Films as a Platform To Guide Neuron-like Differentiation of Human Mesenchymal Stem Cells. *ACS Appl. Mater. Interfaces* **2016**, *8*, 22849−22859.
(27) Yang, M.; Shuai, Y.; Sunderland, K. S.; Mao, C. Ice-Templated Protein Nanoridges Induce Bone Tissue Formation. *Adv. Funct. Mater.* **2017**, *27*, 1703726.
(28) Hakimi, O.; Knight, D. P.; Vollrath, F.; Vadgama, P. Spider and Mulberry Silkworm Silks as Compatible Biomaterials. *Compos. Part B Eng.* **2007**, *38*, 324−337.
(29) Zhao, Z.; Ma, S.; Wu, C.; Li, X.; Ma, X.; Hu, H.; Wu, J.; Wang, Y.; Liu, Z. Chimeric Peptides Quickly Modify the Surface of Personalized 3D Printing Titanium Implants to Promote Osseointegration. *ACS Appl. Mater. Interfaces* **2021**, *13*, 33981−33994.
(30) Zhang, Q.; Ma, L.; Zheng, S.; Wang, Y.; Feng, M.; Shuai, Y.; Duan, B.; Fan, X.; Yang, M.; Mao, C. Air-Plasma Treatment Promotes Bone-like Nano-Hydroxylapatite Formation on Protein Films for Enhanced: In Vivo Osteogenesis. *Biomater. Sci.* **2019**, *7*, 2326−2334.
(31) Ryan, B. J.; Poduska, K. M. Roughness Effects on Contact Angle Measurements. *Am. J. Phys.* **2008**, *76*, 1074−1077.
(32) Yao, X.; Peng, R.; Ding, J. Effects of Aspect Ratios of Stem Cells on Lineage Commitments with and without Induction Media. *Biomaterials* **2013**, *34*, 930−939.
(33) Lee, J.-H.; Choi, H. K.; Yang, L.; Chueng, S.-T. D.; Choi, J.-W.; Lee, K.-B. Nondestructive Real-Time Monitoring of Enhanced Stem Cell Differentiation Using a Graphene-Au Hybrid Nanoelectrode Array. *Adv. Mater.* **2018**, *30*, No. 1802762.
(34) Carreira, A. C.; Lojudice, F. H.; Halcsik, E.; Navarro, R. D.; Sogayar, M. C.; Granjeiro, J. M. Bone Morphogenetic Proteins: Facts, Challenges, and Future Perspectives. *J. Dent. Res.* **2014**, *93*, 335−345.
(35) Shuai, Y.; Lu, H.; Lv, R.; Wang, J.; Wan, Q.; Mao, C.; Yang, M. Biomineralization Directed by Prenucleated Calcium and Phosphorus Nanoclusters Improving Mechanical Properties and Osteogenic Potential of *Antheraea Pernyi* Silk Fibroin-Based Artificial Periosteum. *Adv. Healthcare Mater.* **2021**, *10*, No. 2001695.
(36) Huang, Y.; Wang, X.; Zhou, D.; Zhou, W.; Dai, F.; Lin, H. Macrophages in Heterotopic Ossification: From Mechanisms to Therapy. *Npj Regener. Med.* **2021**, *6*, 70.
(37) Zhang, N.; Song, Y.; Huang, Z.; Chen, J.; Tan, H.; Yang, H.; Fan, M.; Li, Q.; Wang, Q.; Gao, J.; Pang, Z.; Qian, J.; Ge, J. Monocyte Mimics Improve Mesenchymal Stem Cell-Derived Extracellular Vesicle Homing in a Mouse MI/RI Model. *Biomaterials* **2020**, *255*, No. 120168.
(38) Kim, J.; Hematti, P. Mesenchymal Stem Cell−Educated Macrophages: A Novel Type of Alternatively Activated Macrophages. *Exp. Hematol.* **2009**, *37*, 1445−1453.
(39) Lieder, R.; Sigurjonsson, O. E. The Effect of Recombinant Human Interleukin-6 on Osteogenic Differentiation and YKL-40 Expression in Human, Bone Marrow−Derived Mesenchymal Stem Cells. *BioResearch Open Access* **2014**, *3*, 29−34.
(40) Huang, R. L.; Chen, G.; Wang, W.; Herller, T.; Xie, Y.; Gu, B.; Li, Q. Synergy between IL-6 and Soluble IL-6 Receptor Enhances Bone Morphogenetic Protein-2/Absorbable Collagen Sponge-Induced Bone Regeneration via Regulation of BMPRIA Distribution and Degradation. *Biomaterials* **2015**, *67*, 308−322.
(41) Giachelli, C. M.; Steitz, S. Osteopontin: A Versatile Regulator of Inflammation and Biomineralization. *Matrix Biol.* **2000**, *19*, 615−622.
(42) Boskey, A. L. Mineral-Matrix Interactions in Bone and Cartilage. *Clin. Orthop.* **1992**, *281*, 244−274.

https://doi.org/10.1021/acsami.2c17554
ACS Appl. Mater. Interfaces 2023, 15, 7673−7685